


Article

A Nanosensor for Naked-Eye Identification and Adsorption of Cadmium Ion Based on Core–Shell Magnetic Nanospheres

Yaohui Xu ¹, Chi Deng ¹, Zhigang Xiao ¹, Chang Chen ¹, Xufeng Luo ¹, Yang Zhou ^{2,*} 
and Qiang Jiang ^{1,*}

¹ Laboratory for Functional Materials, School of Electronics and Materials Engineering, Leshan Normal University, Leshan 614000, China; xyh1986@lsnu.edu.cn (Y.X.); dengchi@lsnu.edu.cn (C.D.); xiaozhigang@lsnu.edu.cn (Z.X.); chenchang@lsnu.edu.cn (C.C.); luoxufeng@lsnu.edu.cn (X.L.)

² School of Textile Science and Engineering, National Engineering Laboratory for Advanced Yarn and Clean Production, Wuhan Textile University, Wuhan 430200, China

* Correspondence: yzhou@wtu.edu.cn (Y.Z.); jiangqiang@lsnu.edu.cn (Q.J.); Tel.: +86-0833-2276270 (Q.J.)

Received: 7 July 2020; Accepted: 5 August 2020; Published: 20 August 2020



Abstract: Fe₃O₄@SiO₂ nanospheres with a core–shell structure were synthesized and functionalized with bis(2-pyridylmethyl)amine (BPMA). The photoresponses of the as-obtained Fe₃O₄@SiO₂-BPMA for Cr³⁺, Cd²⁺, Hg²⁺ and Pb²⁺ ions were evaluated through irradiation with a 352 nm ultraviolet lamp, and Fe₃O₄@SiO₂-BPMA exhibited remarkable fluorescence enhancement toward the Cd²⁺ ion. The adsorption experiments revealed that Fe₃O₄@SiO₂-BPMA had rapid and effective adsorption toward the Cd²⁺ ion. The adsorption reaction was mostly complete within 30 min, the adsorption efficiency reached 99.3%, and the saturated adsorption amount was 342.5 mg/g based on Langmuir linear fitting. Moreover, Fe₃O₄@SiO₂-BPMA displayed superparamagnetic properties with the saturated magnetization of 20.1 emu/g, and its strong magnetic sensitivity made separation simple and feasible. Our efforts in this work provide a potential magnetic functionalized nanosensor for naked-eye identification and adsorption toward the Cd²⁺ ion.

Keywords: Fe₃O₄@SiO₂; magnetism; fluorescence; adsorption; Cd²⁺

1. Introduction

Cadmium (Cd) is an important rare element, which is widely used in the production of pigments [1], phosphors [2] and photocells [3]. Because of its strong toxicity, the Cd²⁺ ion can cause serious environmental and health issues, including itai-itai disease, lung cancer, renal cancer and prostatic cancer [4–6]. Therefore, some fluorescent chemosensors have been developed for the selective recognition and sensing of the Cd²⁺ ion. These chemosensors can be induced by the Cd²⁺ ion and exhibit naked-eye changes in fluorescence. High sensitivity, high selectivity, instantaneous response and simplicity are the greatest advantages of these probe molecules [7–10]. However, these chemosensors for Cd²⁺ are meant to be disposable and for single use only, and they are difficult if not impossible to recycle. On this basis, the incorporation of fluorescent chemosensors and nanomaterials into an inorganic/organic hybrid nanocomposite is presented.

Magnetic Fe₃O₄@SiO₂ nanoparticles with a core–shell structure have attracted an increasing interest in biological and environmental fields [11–14]. The particles with nano size possess abundant surface active sites for surface modification, and the greatest strength of Fe₃O₄@SiO₂ nanoparticles is their targeting ability. These magnetic particles can be attracted to a target zone under the action of an external magnetic field, which makes recovery feasible [15–21]. Moreover, the inert SiO₂-shell can

prevent the magnetic Fe₃O₄-core from oxidation, and the abundant surface hydroxyl of SiO₂ is highly conducive to surface grafting with organic ligands [22–25].

In this work, we developed an inorganic/organic hybrid nanosensor for Cd²⁺ detection, in which the core–shell Fe₃O₄@SiO₂ nanospheres were employed as a matrix, and bis(2-pyridylmethyl)amine (BPMA) was grafted onto the end of the Fe₃O₄@SiO₂ surface through the “grafting from” method. BPMA is a tridentate ligand with two terminal nitrogen-donor coordination sites (pyridyl) and the central nitrogen donor site (amine), which can coordinate with some heavy metal ions to form complexes. The coordination behavior with metal ions caused an interesting photoresponse, especially ones with d¹⁰ metal centers. The as-obtained Fe₃O₄@SiO₂-BPMA showed a significant change after binding with a Cd²⁺ ion in the excitation of ultraviolet light, which was visible to the naked eye. Moreover, Fe₃O₄@SiO₂-BPMA also showed rapid and efficient adsorption toward the Cd²⁺ ion. It is worth noting that Fe₃O₄@SiO₂-BPMA possesses superparamagnetism, and the strong magnetic sensitivity makes recycling easier.

2. Experimental

2.1. Materials

FeCl₂·4H₂O, FeCl₃·6H₂O, NH₃·H₂O (25 wt.%), trisodium citrate and ethyl silicate were purchased from Shanghai Macklin Biochemical Co. Ltd. (Shanghai, China) Trichloromethylsilane, trichloro(3-chloropropyl)silane, branched polyethylenimine (Mw ~25,000), 4-bromonaphthalic anhydride and bis(2-pyridylmethyl)amine (BPMA) were purchased from Sigma-Aldrich Co. Ltd. (Shanghai, China)

2.2. Synthesis of Fe₃O₄@SiO₂ Nanospheres

Firstly, Fe₃O₄ particles were synthesized based on a chemical co-precipitation strategy. Briefly, FeCl₂·4H₂O (10 mmol) and FeCl₃·6H₂O (20 mmol) were dissolved with distilled water (120 mL), and 60 mL of NH₃·H₂O (25 wt.%) was added to the above solution under a N₂ atmosphere with mechanical stirring. The mixture was kept for 30 min at 70 °C. After that, the black precipitate was collected and washed with distilled water. Subsequently, the as-synthesized Fe₃O₄ particles were added to a trisodium citrate solution (150 mL, 20 mmol/L), the mixture was kept with mechanical stirring for 12 h at room temperature, and N₂ was bubbled throughout the reaction. After that, the citrate-capped Fe₃O₄ was washed with distilled water and ethanol.

Then, Fe₃O₄@SiO₂ particles were synthesized using a sol–gel process by the hydrolysis and condensation of ethyl silicate on the Fe₃O₄ seed. Briefly, the citrate-capped Fe₃O₄ (0.56 g), NH₃·H₂O (5.0 mL, 25 wt.%) and ethyl silicate (4.0 mL) were added to ethanol (120 mL) under mechanical stirring, and the mixture was kept for 8 h at room temperature under a N₂ atmosphere. After that, the as-synthesized Fe₃O₄@SiO₂ precipitate was collected and washed with ethanol.

2.3. Fe₃O₄@SiO₂ Functionalized with BPMA

The surface modifications on Fe₃O₄@SiO₂ are illustrated by a flow chart in Figure 1. Firstly, the Fe₃O₄@SiO₂ surface was functionalized with chlorine groups (labeled as Fe₃O₄@SiO₂-Cl). Fe₃O₄@SiO₂ (0.60 g), trichloromethylsilane (17.6 mmol) and trichloro(3-chloropropyl)silane (1.4 mmol) were added to hexane (150 mL), and the mixture was kept for 24 h with mechanical stirring at room temperature in an atmosphere of hydrogen chloride. After that, the as-synthesized Fe₃O₄@SiO₂-Cl particles were washed with ethanol.

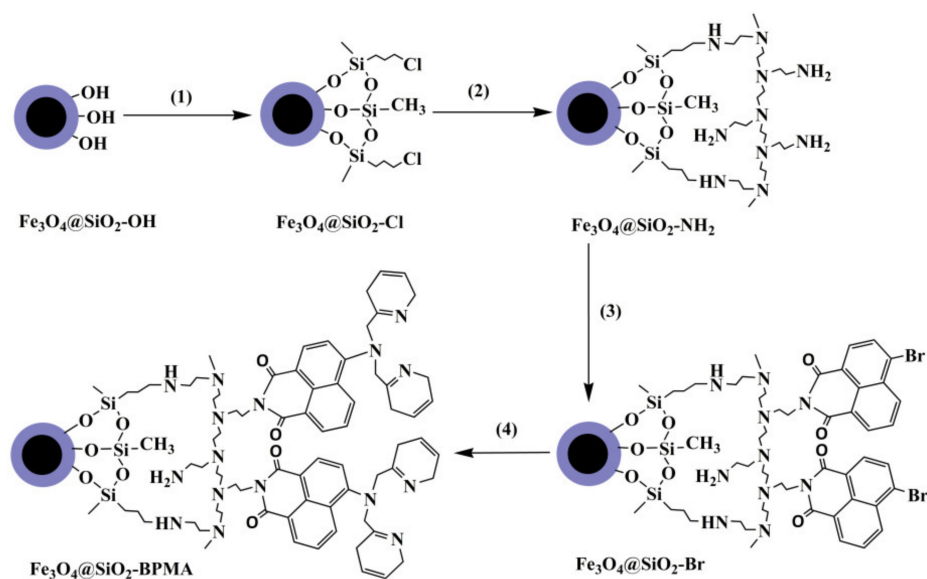


Figure 1. Synthesis of bis(2-pyridylmethyl)amine (BPMA)-functionalized $\text{Fe}_3\text{O}_4@SiO_2$ by a “grafting-from” approach.

Secondly, the $\text{Fe}_3\text{O}_4@SiO_2$ surface was functionalized with amino groups (labeled as $\text{Fe}_3\text{O}_4@SiO_2-NH_2$). The above $\text{Fe}_3\text{O}_4@SiO_2-Cl$, methanol (5.0 mL) and branched polyethylenimine (1.0 mL) were added to distilled water (120 mL) under a N_2 atmosphere with mechanical stirring, and the mixture was kept for 48 h at 65 °C. After that, the as-synthesized $\text{Fe}_3\text{O}_4@SiO_2-NH_2$ particles were washed with distilled water and ethanol.

Thirdly, the $\text{Fe}_3\text{O}_4@SiO_2$ surface was functionalized with bromine groups (labeled as $\text{Fe}_3\text{O}_4@SiO_2-Br$). The above $\text{Fe}_3\text{O}_4@SiO_2-NH_2$ and 4-bromonaphthalic anhydride (5.4 mmol) were added to ethanol (80 mL) under a N_2 atmosphere with mechanical stirring, and the mixture was refluxed for 36 h in darkness. After that, the as-synthesized $\text{Fe}_3\text{O}_4@SiO_2-Br$ particles were washed with ethanol.

Finally, the $\text{Fe}_3\text{O}_4@SiO_2$ surface was functionalized with bis(2-pyridylmethyl)amine (labeled as $\text{Fe}_3\text{O}_4@SiO_2-BPMA$). The above $\text{Fe}_3\text{O}_4@SiO_2-Br$ and BPMA (7.02 mmol) were added to toluene (120 mL) under a N_2 atmosphere with mechanical stirring, and the mixture was refluxed for 36 h in darkness. After that, the as-synthesized $\text{Fe}_3\text{O}_4@SiO_2-BPMA$ particles were washed with ethanol and then dried in vacuum at 60 °C for 24 h.

2.4. Characterization

X-ray diffraction (XRD) analyses were carried out using a DX-2700 instrument (Dandong, China) with $\text{Cu K}\alpha$ radiation (30 kV, 25 mA). Transmission electron microscopy (TEM) and scanning electron microscopy (SEM) images were obtained by means of JEM-2100 (Tokyo, Japan) and SU8020 (Tokyo, Japan) instruments, respectively. Fourier transform infrared (FTIR) spectra were obtained using a Spectrum One (Nicolet iS 10, Waltham, MA, USA). X-ray photoelectron spectroscopy (XPS) analyses were performed by an ESCALAB 250Xi electron spectrometer (Waltham, MA, USA). Magnetization curves were obtained using a vibrating sample magnetometer (VSM, Lakeshore 7307, Columbus, OH, USA).

2.5. Adsorption Study

The adsorption capacities of $\text{Fe}_3\text{O}_4@SiO_2-BPMA$ were evaluated by removing heavy metal ions with strong toxicity (Cr^{3+} , Cd^{2+} , Hg^{2+} and Pb^{2+} ions) from simulated wastewaters. Briefly, 50 mg $\text{Fe}_3\text{O}_4@SiO_2$ or $\text{Fe}_3\text{O}_4@SiO_2-BPMA$ powders were dispersed in 50 mL of the simulated wastewaters without pH pre-adjustments. The mixture was stirred with a constant speed at room temperature.

Then, a certain amount of suspension was withdrawn at regular intervals, and the qualitative analysis of metal ions was performed. The adsorption efficiencies (η_t , %) at a time t were calculated using Equation (1).

$$\eta_t = \frac{C_0 - C_t}{C_0} \times 100 \% \quad (1)$$

3. Results and Discussion

Figure 2 shows the XRD patterns of Fe_3O_4 and $\text{Fe}_3\text{O}_4@\text{SiO}_2$ powders. As observed, the XRD patterns of Fe_3O_4 showed several well-resolved peaks indexed to (220), (311), (400), (422), (511) and (440) planes, which are considered strongly consistent with the database of magnetite (JCPDS No. 65-3107). According to the Scherrer formula, the grain size of Fe_3O_4 was calculated, and the value was about 9.6 nm. For the XRD pattern of $\text{Fe}_3\text{O}_4@\text{SiO}_2$, besides the diffraction peaks of the Fe_3O_4 phase, a broad and weak peak at $2\theta = 11\sim 27^\circ$ (the orange dotted bordered rectangle) was observed, which was assigned to amorphous SiO_2 . This suggests that the Fe_3O_4 crystal was successfully composited with amorphous SiO_2 .

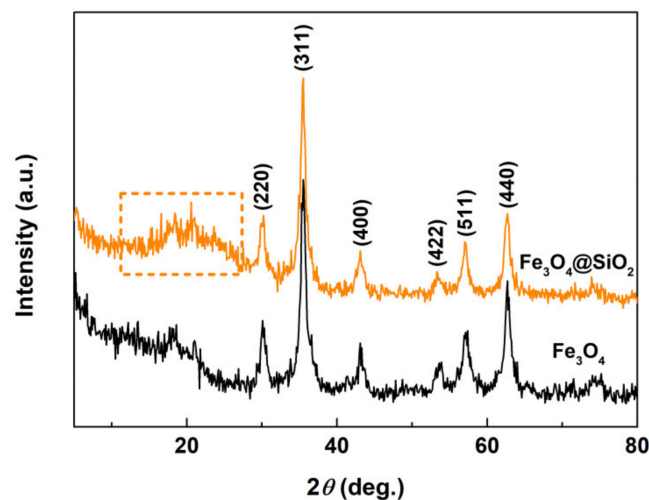


Figure 2. XRD patterns of Fe_3O_4 and $\text{Fe}_3\text{O}_4@\text{SiO}_2$ powders.

Figure 3a shows the TEM image of Fe_3O_4 particles. As observed, the Fe_3O_4 particles exhibited a mean size of about 10 nm, consistent with the calculation of XRD analysis. After compositing with SiO_2 , the size of particles increased to about 24.0 nm, as shown in the SEM image in Figure 3b, and the TEM image in Figure 3c reveals the obvious core-shell structure with a shell thickness of about 7.0 nm. This suggests that $\text{Fe}_3\text{O}_4@\text{SiO}_2$ nanospheres with a core-shell structure were successfully synthesized using a sol-gel process by the hydrolysis and condensation of ethyl silicate on the Fe_3O_4 seed. However, the $\text{Fe}_3\text{O}_4@\text{SiO}_2$ particles were aggregated slightly, which may be attributed to the enhancement of surface activity after coating SiO_2 on the Fe_3O_4 seed because of more abundant surface hydroxyl from SiO_2 . Figure 3d,e show the SEM and TEM images of $\text{Fe}_3\text{O}_4@\text{SiO}_2$ -BPMA particles, respectively. There were no significant changes in either size or morphology compared with those of $\text{Fe}_3\text{O}_4@\text{SiO}_2$ particles.

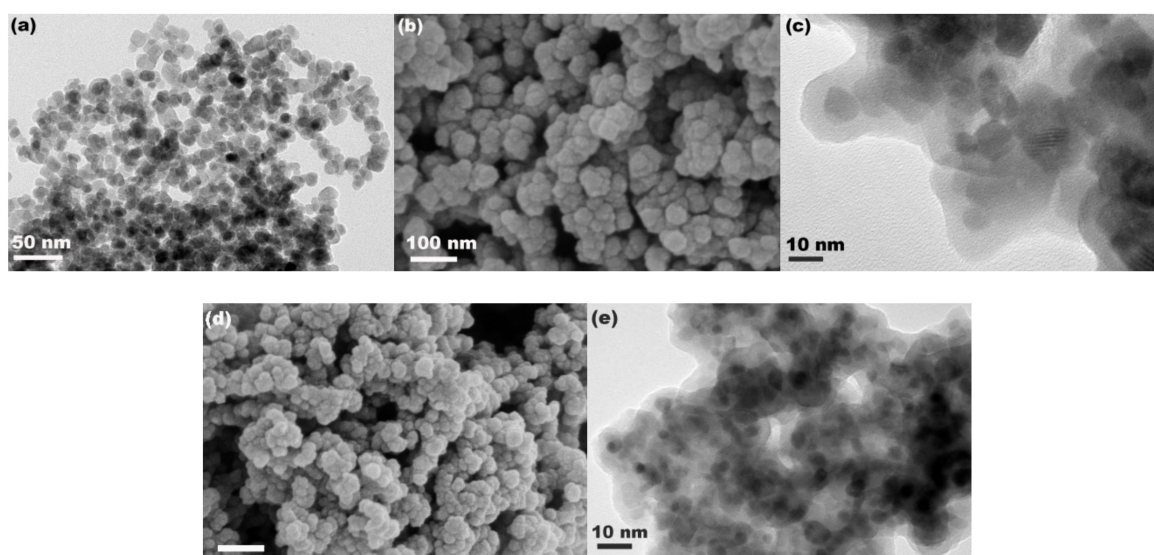


Figure 3. (a) TEM image of Fe_3O_4 particles, (b) SEM and (c) TEM images of $\text{Fe}_3\text{O}_4@SiO_2$ particles, (d) SEM and (e) TEM images of $\text{Fe}_3\text{O}_4@SiO_2\text{-BPMA}$ particles.

The grafted groups on the $\text{Fe}_3\text{O}_4@SiO_2$ surface were characterized by FTIR. As observed in Figure 4a–e, the peaks for all samples at 3437, 1086 and 576 cm^{-1} were ascribed to the stretching vibration of O–H, Si–O and Fe–O bonds, further demonstrating the successful synthesis of $\text{Fe}_3\text{O}_4@SiO_2$ with abundant surface hydroxyl. In the FTIR spectrum of $\text{Fe}_3\text{O}_4@SiO_2\text{-Cl}$ (Figure 4b), the absorption peaks at 2972 and 1272 cm^{-1} were ascribed to the stretching of C–H species and the symmetrical deformation vibration of Si–C species, respectively. Compared with the FTIR spectrum of $\text{Fe}_3\text{O}_4@SiO_2\text{-Cl}$, there were no observable changes in that of $\text{Fe}_3\text{O}_4@SiO_2\text{-NH}_2$ in Figure 4c, but the signal of the Si–O bond vanished at 576 cm^{-1} . For the FTIR spectrum of $\text{Fe}_3\text{O}_4@SiO_2\text{-Br}$ in Figure 4d, the absorption peaks at 1704, 1654 and 1339 cm^{-1} could be attributable to N–C=O species. In Figure 4d, the immobilization of BPMA on the $\text{Fe}_3\text{O}_4@SiO_2$ surface is demonstrated by the new peak appearing at 1590 cm^{-1} , which could be attributable to C=N species. Further analyses of $\text{Fe}_3\text{O}_4@SiO_2\text{-BPMA}$ were conducted by XPS, as discussed below.

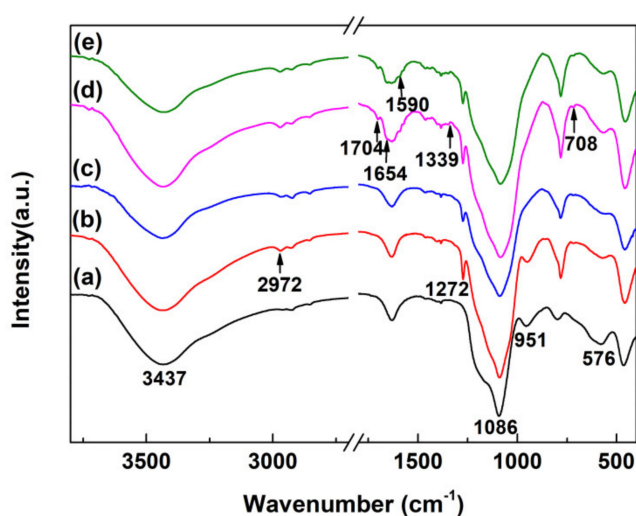


Figure 4. FTIR spectra of (a) $\text{Fe}_3\text{O}_4@SiO_2$, (b) $\text{Fe}_3\text{O}_4@SiO_2\text{-Cl}$, (c) $\text{Fe}_3\text{O}_4@SiO_2\text{-NH}_2$, (d) $\text{Fe}_3\text{O}_4@SiO_2\text{-Br}$ and (e) $\text{Fe}_3\text{O}_4@SiO_2\text{-BPMA}$ powders.

Figure 5a,b show the XPS spectra of C 1s and N 1s core-levels of $\text{Fe}_3\text{O}_4@SiO_2\text{-BPMA}$ powders, respectively. As observed in Figure 5a, the C 1s core-level spectrum of $\text{Fe}_3\text{O}_4@SiO_2\text{-BPMA}$ can be

curve-fitted into five peak components with binding energies of 287.9, 286.0, 285.3, 284.7 and 284.1 eV, corresponding to C=O, C-N, C-C, (C₆H₅-) and C-Si bonds, respectively. Moreover, the N 1s core-level spectrum in Figure 5b can be curve-fitted into three peak components with the binding energies of 401.1 eV for pyridinic-N species, 399.8 eV for N-C species and 399.0 eV for N-C=O species, respectively. Combined with the results of FTIR analyses in Figure 4, it can be concluded that BPMA was successfully bonded onto the Fe₃O₄@SiO₂ surface through a series of successive coupling reactions.

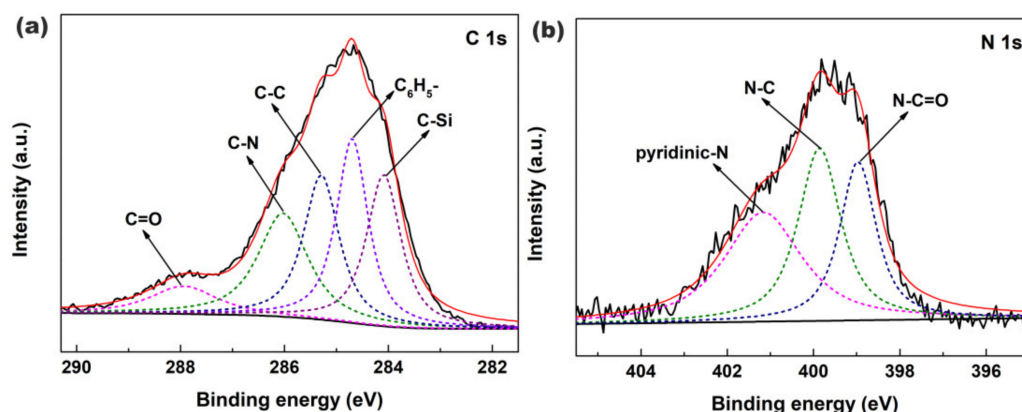


Figure 5. XPS spectra of (a) C 1s and (b) N 1s core-levels of Fe₃O₄@SiO₂-BPMA powders.

The magnetic properties of Fe₃O₄@SiO₂ and Fe₃O₄@SiO₂-BPMA powders were investigated using a VSM at 300 K. As observed in Figure 6, the saturated magnetization of Fe₃O₄@SiO₂ and Fe₃O₄@SiO₂-BPMA powders were 38.1 and 20.1 emu/g with neither remanence nor coercivity, indicating their superparamagnetism. Compared with Fe₃O₄@SiO₂, the decrease in saturated magnetization for Fe₃O₄@SiO₂-BPMA powders was attributed to the contribution of the non-magnetic grafted organic molecule on the Fe₃O₄@SiO₂ surface. The insets in Figure 6 show the photographs of the magnetic response using a magnet and re-dispersion by shaking the Fe₃O₄@SiO₂-BPMA suspension. From the Figure 6 insets, it can be seen that Fe₃O₄@SiO₂-BPMA particles were well dispersed in an aqueous solution, and these particles were quickly and completely separated from solution under the attraction of an external magnet within about 30 seconds in this work. Moreover, the re-dispersion of Fe₃O₄@SiO₂-BPMA in aqueous solution occurred simply and quickly through slight shaking once the external magnet was removed. This demonstrates that the as-synthesized Fe₃O₄@SiO₂-BPMA possesses strong magnetic sensitivity, which could make recycling easy and feasible.

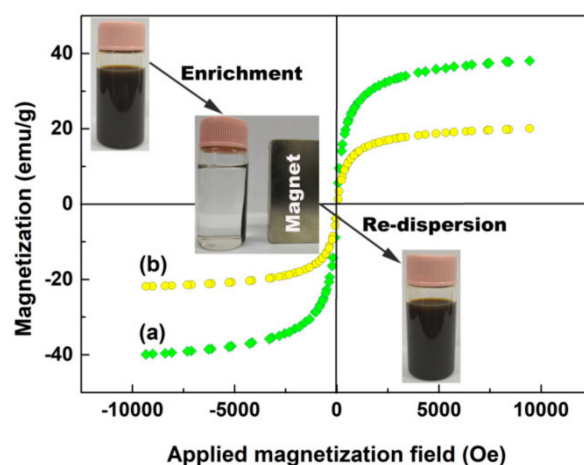


Figure 6. Magnetization hysteresis loops of Fe₃O₄@SiO₂ (a) and Fe₃O₄@SiO₂-BPMA (b) powders (insets are the Fe₃O₄@SiO₂-BPMA suspension, [Fe₃O₄@SiO₂-BPMA] = 1.25 g/L, V = 8.0 mL, aqueous medium).

To evaluate the photoresponse of the $\text{Fe}_3\text{O}_4@\text{SiO}_2\text{-BPMA}$ nanosensor for heavy metal ions such as Cr^{3+} , Cd^{2+} , Hg^{2+} and Pb^{2+} ions, the fluorescence changes to various heavy metal ions with equal concentrations were measured using a 352 nm fluorescent lamp. The top of Figure 7 shows the changes in color of the $\text{Fe}_3\text{O}_4@\text{SiO}_2\text{-BPMA}$ suspension upon the addition of Me^{n+} ($\text{Me}^{n+} = \text{Cr}^{3+}$, Cd^{2+} , Hg^{2+} and Pb^{2+}) illuminated by natural light; the $\text{Fe}_3\text{O}_4@\text{SiO}_2\text{-BPMA}$ suspension had no significant changes in the appearance of color after the addition of Cr^{3+} , Cd^{2+} , Hg^{2+} and Pb^{2+} ions in comparison with that of only $\text{Fe}_3\text{O}_4@\text{SiO}_2\text{-BPMA}$ (blank in Figure 7, top). The bottom of Figure 7 shows the eye-perceived fluorescence changes in $\text{Fe}_3\text{O}_4@\text{SiO}_2\text{-BPMA}$ toward Cr^{3+} , Cd^{2+} , Hg^{2+} and Pb^{2+} ions through irradiation with a 352 nm ultraviolet lamp. The considerable fluorescence enhancements can be observed by the naked eye in the vial with the Cd^{2+} ion, and the detection limit for Cd^{2+} ions reached up to 8.0×10^{-7} mol/L. In contrast, no significant fluorescent changes in emission were observed for the other vials containing Cr^{3+} , Hg^{2+} and Pb^{2+} ions. However, the coordination diagrammatic sketch of $\text{Fe}_3\text{O}_4@\text{SiO}_2\text{-BPMA}$ with Cd^{2+} is shown in Figure 8. Upon the addition of the Cd^{2+} ion, the grafted tridentate receptor BPMA molecule coordinated with the Cd^{2+} ion, which decreased the electron-donating ability of the nitrogen atom from BPMA during the photo-induced charge transfer process, and thus, significant fluorescence enhancement occurred [26–28].

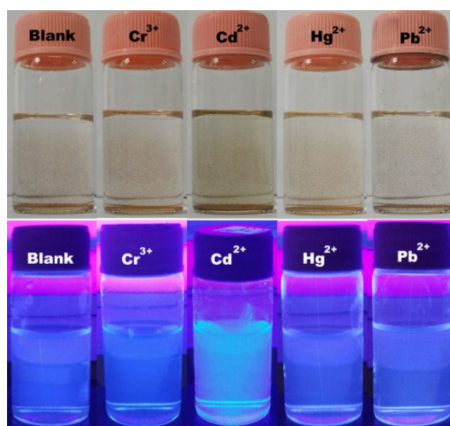


Figure 7. Changes in color (top) illuminated by natural light and fluorescence (bottom) illuminated with a fluorescent lamp ($\lambda_{\text{ex}} = 352$ nm, 8 W) of $\text{Fe}_3\text{O}_4@\text{SiO}_2\text{-BPMA}$ upon the addition of Me^{n+} ($\text{Me}^{n+} = \text{Cr}^{3+}$, Cd^{2+} , Hg^{2+} and Pb^{2+}) ($[\text{Fe}_3\text{O}_4@\text{SiO}_2\text{-BPMA}] = 0.1$ g/L; $[\text{Me}^{n+}] = 10^{-5}$ mol/L; $V = 6$ mL, $V_{\text{acetonitrile}}/V_{\text{water}} = 4/1$).

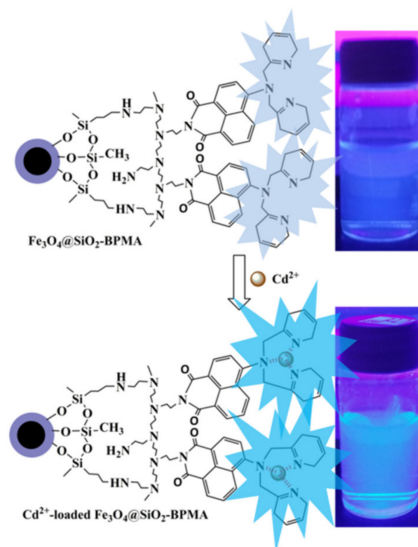


Figure 8. Binding mechanism of $\text{Fe}_3\text{O}_4@\text{SiO}_2\text{-BPMA}$ toward Cd^{2+} ions.

The adsorption capacity of Fe₃O₄@SiO₂-BPMA nanocomposites toward the Cd²⁺ ion was evaluated at room temperature without pH pre-adjustments. Figure 9 shows the time-dependence of adsorption profiles of the Cd²⁺ ion onto Fe₃O₄@SiO₂-BPMA. As observed, Fe₃O₄@SiO₂-BPMA exhibited rapid adsorption to Cd²⁺ ions within 20 min, and the adsorption efficiency within 20 min reached 90.5%. Moreover, the adsorption reaction was mostly complete within 30 min, and the adsorption efficiency within 30 min reached 99.3%. As a comparison, the adsorption capacity of Fe₃O₄@SiO₂ without BPMA modification was also tested, and the adsorption efficiency within 60 min was below 5.0% under the same conditions. This indicates that the adsorption of the Cd²⁺ ion was mainly attributed to the grafted BPMA molecule, not Fe₃O₄@SiO₂ particles.

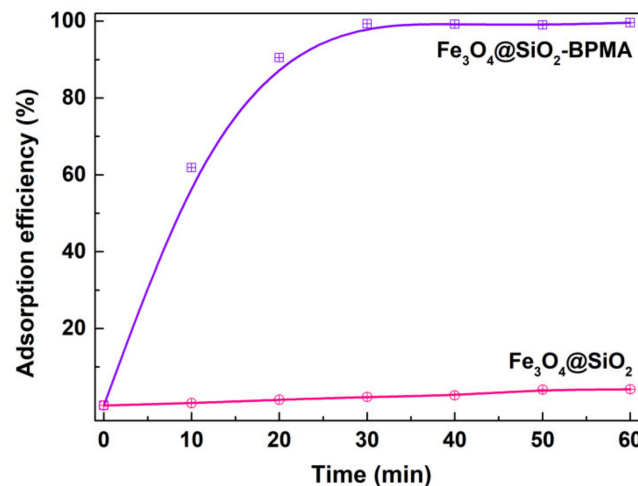


Figure 9. Time-dependence of adsorption profiles of Cd²⁺ ion onto Fe₃O₄@SiO₂ and Fe₃O₄@SiO₂-BPMA powders (adsorption conditions: room temperature; no pH pre-adjustments; [Fe₃O₄@SiO₂-BPMA] = 1.0 g/L; [Cd²⁺] = 200 mg/L; V = 50 mL; t = 0–60 min).

Figure 10 shows the effects of Cd²⁺ initial concentration on the adsorption efficiency and adsorption amount of the Fe₃O₄@SiO₂-BPMA adsorbent. As observed, the adsorption efficiency decreased with the increasing Cd²⁺ initial concentration, the decrease being especially sharp when the Cd²⁺ initial concentration was higher than 300 mg/L, which could be due to the saturation of the Fe₃O₄@SiO₂-BPMA adsorbent. The adsorption efficiency remained at more than 94.0% when the Cd²⁺ initial concentration was lower than 300 mg/L. However, the adsorption amount increased with the increasing Cd²⁺ initial concentration, and the increasing trend receded gradually. The mass of the Fe₃O₄@SiO₂-BPMA adsorbent was certain, and the relative adsorption sites gradually decreased with the increasing Cd²⁺ initial concentration and finally reached an adsorption–desorption equilibrium between the Cd²⁺ ion and the adsorbent. The saturated adsorption amount (q_m , mg/g) of Cd²⁺ ions can be evaluated by the Langmuir isotherm model using Equations (2) and (3).

$$q_e = \frac{(C_0 - C_e)V}{m} \quad (2)$$

$$\frac{C_e}{q_e} = \frac{1}{q_m} C_e + \frac{1}{K_L q_m} \quad (3)$$

where C_0 (mg/L) is the initial concentration of Cd²⁺ ions, C_e (mg/L) is the concentration of Cd²⁺ ions at equilibrium, m (g) is the mass of Fe₃O₄@SiO₂-BPMA powders, V (L) is the volume of Cd²⁺ aqueous solution, q_e (mg/g) is the equilibrium adsorption amount of Fe₃O₄@SiO₂-BPMA, q_m (mg/g) is the saturated adsorption amount of Fe₃O₄@SiO₂-BPMA, and K_L is the Langmuir adsorption constant. The Langmuir linear fit of the adsorption of Cd²⁺ ions onto Fe₃O₄@SiO₂-BPMA is shown in Figure 11. The corresponding Langmuir parameters calculated at room temperature were as follows:

$q_m = 342.5$ mg/g and $K_L = 0.5478$. Moreover, a high associated correlation coefficient R^2 of 0.9991 was obtained, indicating that the Langmuir isotherm model was a good fit for modeling the adsorption of Cd^{2+} ions onto $\text{Fe}_3\text{O}_4@\text{SiO}_2\text{-BPMA}$.

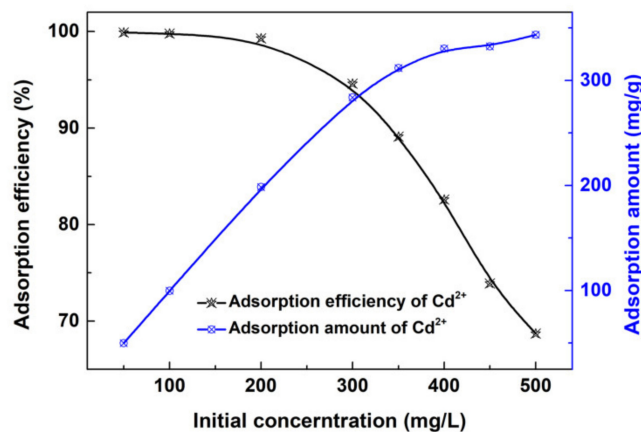


Figure 10. Effects of Cd^{2+} initial concentration on the adsorption efficiency and adsorption amount (adsorption conditions: room temperature; no pH pre-adjustments; $[\text{Fe}_3\text{O}_4@\text{SiO}_2\text{-BPMA}] = 1.0$ g/L; $[\text{Cd}^{2+}] = 50\text{--}500$ mg/L; $V = 50$ mL; $t = 30$ min).

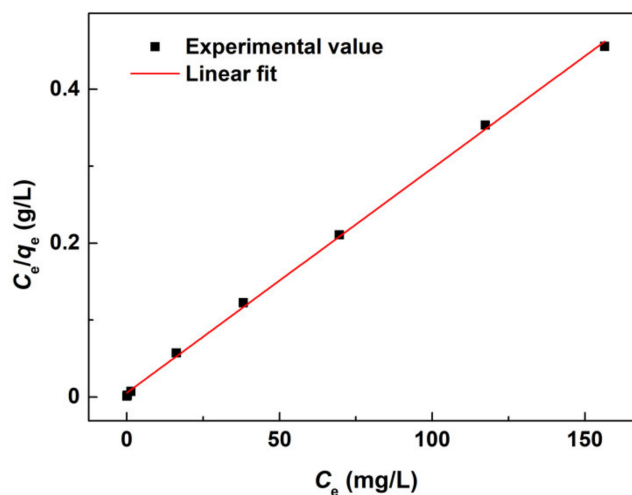


Figure 11. Langmuir linear fit of Cd^{2+} adsorbed onto $\text{Fe}_3\text{O}_4@\text{SiO}_2\text{-BPMA}$.

4. Conclusions

A sensitive fluorescence sensor based on functionalized $\text{Fe}_3\text{O}_4@\text{SiO}_2$ nanospheres was used for simultaneously detecting and removing Cd^{2+} ions. The as-synthesized $\text{Fe}_3\text{O}_4@\text{SiO}_2\text{-BPMA}$ underwent an eye-perceived fluorescence enhancement induced by Cd^{2+} ions. Meanwhile, $\text{Fe}_3\text{O}_4@\text{SiO}_2\text{-BPMA}$ exhibited rapid and effective adsorption toward the Cd^{2+} ion, and the adsorption reaction was mostly complete within 30 min. The Cd^{2+} adsorption capacity of $\text{Fe}_3\text{O}_4@\text{SiO}_2\text{-BPMA}$ was determined by fitting the experimental data with the Langmuir model, and the saturated adsorption amount was 342.5 mg/g at room temperature. Moreover, $\text{Fe}_3\text{O}_4@\text{SiO}_2\text{-BPMA}$ showed superparamagnetic properties with a saturated magnetization of 20.1 emu/g, which could help to separate these particles after capturing Cd^{2+} ions. The nanocomposites presented here have great potential applications for the naked-eye identification, adsorption and separation of the Cd^{2+} ion.

Author Contributions: Y.X. project administration; writing—original draft preparation; Z.X. and C.C. data curation; X.L., formal analysis; Q.J. funding acquisition; Y.Z. and C.D. supervision. All authors have read and agreed to the published version of the manuscript.

Funding: This research was funded by Leshan Normal University Research Program, China (No. LZD021).

Conflicts of Interest: The authors declare no conflict of interest.

References

1. Makarewicz, E.; Cysewski, P.; Michalik, A.; Ziółkowska, D. Properties of Acid or Alkali Treated Cadmium Pigments. *Dyes Pigment.* **2013**, *96*, 338–348. [[CrossRef](#)]
2. İlhan, M.; Keskin, İ.Ç. Photoluminescence, Radioluminescence and Thermoluminescence Properties of Eu³⁺ Doped Cadmium Tantalate Phosphor. *Dalton Trans.* **2018**, *47*, 13939–13948. [[CrossRef](#)]
3. Ma, J.; Ni, S.; Zhang, J.; Yang, X.; Zhang, L. The Electrochemical Performance of Nickel Chromium Oxide as a New Anode Material for Lithium Ion Batteries. *Electrochim. Acta* **2015**, *176*, 1420–1426. [[CrossRef](#)]
4. Vizuete, J.; Pérez-López, M.; Míguez-Santiyán, M.P.; Hernández-Moreno, D. Mercury (Hg), Lead (Pb), Cadmium (Cd), Selenium (Se), and Arsenic (As) in Liver, Kidney, and Feathers of Gulls: A Review. In *Reviews of Environmental Contamination and Toxicology Volume 247*; Springer International Publishing: Cham, Switzerland, 2008; Volume 247, pp. 85–146. [[CrossRef](#)]
5. Ur Rehman, M.Z.; Rizwan, M.; Hussain, A.; Saqib, M.; Ali, S.; Sohail, M.I.; Shafiq, M.; Hafeez, F. Alleviation of Cadmium (Cd) Toxicity and Minimizing its Uptake in Wheat (*Triticum Aestivum*) by Using Organic Carbon Sources in Cd-Spiked Soil. *Environ. Pollut.* **2018**, *241*, 557–565. [[CrossRef](#)] [[PubMed](#)]
6. D’Haese, P.C.; Couttenye, M.M.; Lamberts, L.V.; Elseviers, M.M.; Goodman, W.G.; Schrooten, I.; Cabrera, W.E.; De Broe, M.E. Aluminum, Iron, Lead, Cadmium, Copper, Zinc, Chromium, Magnesium, Strontium, and Calcium Content in Bone of End-Stage Renal Failure Patients. *Clin. Chem.* **1999**, *45*, 1548–1556. [[CrossRef](#)] [[PubMed](#)]
7. Shi, Y.S.; Li, Y.H.; Cui, G.H.; Dong, G.Y. New Two-Dimensional Cd(II) Coordination Networks Bearing Benzimidazolyl-Based Linkers as Bifunctional Chemosensors for Detection of Acetylacetone and Fe³⁺. *CrystEngComm* **2020**, *22*, 905–914. [[CrossRef](#)]
8. Quan, C.; Liu, J.; Sun, W.; Cheng, X. Highly Sensitive and Selective Fluorescence Chemosensors Containing Phenanthroline Moieties for Detection of Zn²⁺ and Cd²⁺ Ions. *Chem. Pap.* **2019**, *74*, 485–497. [[CrossRef](#)]
9. Eseola, A.O.; Görls, H.; Bangesh, M.; Plass, W. ESIPT-capable 2,6-di(1H-imidazol-2-yl)phenols with Very Strong Fluorescent Sensing Signals towards Cr(III), Zn(II) and Cd(II): Molecular Variation Effects on Turn-On Efficiency. *New J. Chem.* **2018**, *42*, 7884–7900. [[CrossRef](#)]
10. Vera, M.; Santacruz Ortega, H.; Inoue, M.; Machi, L. Bichromophoric Naphthalene Derivatives of Diethylenetriaminepentaacetate (DTPA): Fluorescent Response to H⁺, Ca²⁺, Zn²⁺, and Cd²⁺. *Supramol. Chem.* **2019**, *31*, 336–348. [[CrossRef](#)]
11. Sun, M.; Zhao, A.; Wang, D.; Wang, J.; Chen, P.; Sun, H. Cube-like Fe₃O₄@SiO₂@Au@Ag Magnetic Nanoparticles: A Highly Efficient SERS Substrate for Pesticide Detection. *Nanotechnology* **2018**, *29*, 165302. [[CrossRef](#)]
12. Yuan, Z.; Xu, R.; Li, J.; Chen, Y.; Wu, B.; Feng, J.; Chen, Z. Biological Responses to Core-Shell-Structured Fe₃O₄@SiO₂-NH₂ Nanoparticles in Rats by a Nuclear Magnetic Resonance-Based Metabonomic Strategy. *Int. J. Nanomed.* **2018**, *13*, 2447–2462. [[CrossRef](#)] [[PubMed](#)]
13. Chen, S.; Chen, J.; Zhu, X. Solid Phase Extraction of Bisphenol A Using Magnetic Core-Shell (Fe₃O₄@SiO₂) Nanoparticles Coated with an Ionic liquid, and its Quantitation by HPLC. *Microchim. Acta* **2016**, *183*, 1315–1321. [[CrossRef](#)]
14. Jiang, H.; Liu, Y.; Luo, W.; Wang, Y.; Tang, X.; Dou, W.; Cui, Y.; Liu, W. A Resumable Two-Photon Fluorescent Probe for Cu²⁺ And S²⁻ Based on Magnetic Silica Core-Shell Fe₃O₄@SiO₂ Nanoparticles and its Application in Bioimaging. *Anal. Chim. Acta* **2018**, *1014*, 91–99. [[CrossRef](#)] [[PubMed](#)]
15. Yang, Y.; Liu, Y.; Cheng, C.; Shi, H.; Yang, H.; Yuan, H.; Ni, C. Rational Design of GO-Modified Fe₃O₄/SiO₂ Nanoparticles with Combined Rhenium-188 and Gambogic Acid for Magnetic Target Therapy. *ACS Appl. Mater. Interfaces* **2017**, *9*, 28195–28208. [[CrossRef](#)] [[PubMed](#)]
16. Ding, Z.; Shaw, L.L. Enhancement of Hydrogen Desorption from Nano-Composite Prepared by Ball-Milling MgH₂ with in-situ Aerosol-Spraying LiBH₄. *ACS Sustain. Chem. Eng.* **2019**, *7*, 15064–15072. [[CrossRef](#)]
17. Morita, Y.; Sakurai, R.; Wakimoto, T.; Kobayashi, K.; Xu, B.; Toku, Y.; Song, G.; Luo, Q.; Ju, Y. tLyP-1-Conjugated Core-Shell Nanoparticles, Fe₃O₄NPs@mSiO₂, for Tumor-Targeted Drug Delivery. *Appl. Surf. Sci.* **2019**, *474*, 17–24. [[CrossRef](#)]

18. Ding, Z.; Li, H.; Shaw, L. New Insights into the Solid-State Hydrogen Storage of Nanostructured LiBH₄-MgH₂ System. *Chem. Eng. J.* **2019**, *385*, 123856. [[CrossRef](#)]
19. Du, Q.; Zhang, W.; Ma, H.; Zheng, J.; Zhou, B.; Li, Y. Immobilized Palladium on Surface-Modified Fe₃O₄/SiO₂ Nanoparticles: As a Magnetically Separable and Stable Recyclable High-Performance Catalyst for Suzuki and Heck Cross-Coupling Reactions. *Tetrahedron* **2012**, *68*, 3577–3584. [[CrossRef](#)]
20. Ding, Z.; Lu, Y.; Li, L.; Shaw, L. High Reversible Capacity Hydrogen Storage Through Nano-LiBH₄ + Nano-MgH₂ System. *Energy Storage Mater.* **2019**, *20*, 24–35. [[CrossRef](#)]
21. Zhang, S.; Tang, Y.; Nguyen, L.; Zhao, Y.; Wu, Z.; Goh, T.W.; Liu, J.J.; Li, Y.; Zhu, T.; Huang, W.; et al. Catalysis on Singly Dispersed Rh Atoms Anchored on an Inert Support. *ACS Catal.* **2017**, *8*, 110–121. [[CrossRef](#)]
22. Ding, Z.; Chen, Z.; Ma, T.; Lu, C.-T.; Ma, W.; Shaw, L. Predicting the Hydrogen Release Ability of LiBH₄-based Mixtures by Ensemble Machine Learning. *Energy Storage Mater.* **2019**. [[CrossRef](#)]
23. Peralta-Perez, M.R.; Saucedo-Castañeda, G.; Gutierrez-Rojas, M.; Campero, A. SiO₂ Xerogel: A Suitable Inert Support for Microbial Growth. *J. Sol-Gel Sci. Technol.* **2001**, *20*, 105–110. [[CrossRef](#)]
24. Ding, Z.; Ma, W.; Wei, K.; Wu, J.; Zhou, Y.; Xie, K. Boron Removal from Metallurgical-Grade Silicon Using Lithium Containing Slag. *J. Non-Cryst. Solids* **2012**, *358*, 2708–2712. [[CrossRef](#)]
25. Wu, Y.; Ma, J.; Liu, C.; Yan, H. Surface Modification Design for Improving the Strength and Water Vapor Permeability of Waterborne Polymer/SiO₂ Composites: Molecular Simulation and Experimental Analyses. *Polymers* **2020**, *12*, 170. [[CrossRef](#)] [[PubMed](#)]
26. Eom, G.H.; Kim, J.H.; Jo, Y.D.; Kim, E.Y.; Bae, J.M.; Kim, C.; Kim, S.J.; Kim, Y. Anion Effects on Construction of Cadmium(II) Compounds with A Chelating Ligand Bis(2-Pyridylmethyl)Amine: Their Photoluminescence and Catalytic Activities. *Inorg. Chim. Acta* **2012**, *387*, 106–116. [[CrossRef](#)]
27. Davies, C.J.; Solan, G.A.; Fawcett, J. Synthesis and Structural Characterisation of Cobalt(II) and Iron(II) Chloride Complexes Containing Bis(2-Pyridylmethyl)Amine and Tris(2-Pyridylmethyl)Amine Ligands. *Polyhedron* **2004**, *23*, 3105–3114. [[CrossRef](#)]
28. Park, B.K.; Lee, S.H.; Lee, E.Y.; Kwak, H.; Lee, Y.M.; Lee, Y.J.; Jun, J.Y.; Kim, C.; Kim, S.J.; Kim, Y. Zinc(II) polymeric compounds with a chelating ligand bis(2-pyridylmethyl)amine (bispicam) directed by intermolecular C/N/O–H···X (X=Cl, Br, I) interactions: Catalytic Activities. *J. Mol. Struct.* **2008**, *890*, 123–129. [[CrossRef](#)]

